Proceedings World Geothermal Congress 2020+1
Reykjavik, Iceland, April - October 2021

St1 Deep Heat EGS Project -- Computation of wellbore-to-wellbore permeability stimulation

Peter Leary[1)], Peter Malin[1)], Tero Saarno[2)], Pekka Heikkinen[2)]

1) Advanced Seismic Instrument & Research, 1311 Waterside, Dallas, TX 75218-4475, USA

2)St1 Deep Heat Oy, Purotie 1/PL 100, 00381 Helsinki Finland

Keywords: EGS, permeability, stimulation, fractures

ABSTRACT

A 6km-deep Enhanced/Engineered Geothermal System (EGS) doublet in crystalline rock will be completed in 2019 at the Otaniemi district heating plant 15km west of Helsinki, Finland. An existing 3.3km deep well is to be drilled to 6km depth to parallel the 6km deep well that was recently stimulated by pressure- and flow-rate-controlled injection of 18000 m^3 of fresh water over a 50-day period. The seismicity induced by the injected water was conspicuously not accompanied by large-scale discrete stress-aligned planar fractures to serve as a heat-exchanger leg in an EGS heat extraction flow cycle. Instead, the induced seismicity gave evidence of reactivating fossilised flow pathways characteristic of ambient crustal reservoir flow systems. The Deep Heat project can apply joint well pressurisation aimed at focusing stress in the interwell crustal volume in order to enhance permeability along heat-exchange fluid pathways between the injector-producer well pair.

We numerically simulate the mechanics of pressure-induced EGS permeability enhancement within a thin cylindrical section of poroperm crust perforated by two wellbores. The model poroperm properties are conditioned by quantitative empirics from crystalline rock well-log, well-core, well-temperature and well-stimulation data: (i) spatially-correlated porosity attested by well-log power-spectral scaling, $S_\varphi(k) \sim 1/k$ for spatial frequencies 1/km < k < 1/m; (ii) well-core poroperm spatial correlation $\kappa \sim exp(\alpha\varphi)$ with empirical parameter α having ambient values such that $\alpha\underline{\varphi} \sim$ 3-4 for porosity $\underline{\varphi} \sim$ 0.01; (iii) wellbore-centric Peclet number $P_e \equiv r_0 v_0 \underline{\varphi}/D \sim 10$ observed at 1.5km depth for heat advected by isolated naturally-occurring fracture-connectivity structures in basement rock (r_0 = wellbore radius, v_0 = fluid velocity at wellbore, $\underline{\varphi}$ = mean formation porosity, and D = thermal diffusivity of rock-fluid system); (iv) fluid injection flow rates ~ 10L/s at 70-90MPa wellbore pressure; (v) induced microseismicity with spatial correlation scaling function $G(r) \sim 1/r^{1/2}$, 30m < r < 500m, derivable from empirics (i)-(ii). Generation of permeability stimulation fluid pathways constrained by this suite of spatially-correlated rock-fluid interaction empirics is hypothesised in place of non-existent large-scale discrete fractures of standard permeability stimulation scenario.

Aspects of our computational and observational exercise for EGS stimulation of wellbore-pair crystalline rock volumes at 6km depth are (i) the wellbore-centric radius at which interwell-offset joint pressurisation is effective for presently achievable wellbore pressures; (ii) the degree of permeability enhancement achieved with joint wellbore pressurisation; (iii) the relation between near-wellbore permeability enhancement and induced microseismicity. Sustained interwell flow of Peclet number $P_e \sim 5$ along substantial portions of km-length wellbore-pairs appears feasible for commercial heat supply to the Otaniemi district heating plant. Present results imply a formidable barrier to $P_e \sim 75$ wellbore-to-wellbore heat extraction for electrical power once commonly considered as an achievable EGS target.

1. INTRODUCTION

A 6km-deep Enhanced/Engineered Geothermal System (EGS) doublet in crystalline rock will be completed in 2019 at the Otaniemi district heating plant 15km west of Helsinki, Finland. An existing 3.3km deep well is to be drilled to 6km depth to parallel the 6km deep well that was recently stimulated by pressure- and flow-rate-controlled injection of 18000 m^3 of fresh water over a 50-day period. The seismicity induced by the injected water was conspicuously not accompanied by large-scale discrete stress-aligned planar fractures to serve as a heat-exchanger leg in an EGS heat extraction flow cycle. Instead, the induced seismicity gave evidence of reactivating fossilised flow pathways characteristic of ambient crustal reservoir flow systems. The Deep Heat project can apply joint well pressurisation aimed at focusing stress in the interwell crustal volume in order to enhance permeability along heat-exchange fluid pathways between the injector-producer well pair.

We numerically simulate the mechanics of pressure-induced EGS permeability enhancement within a thin cylindrical section of poroperm crust perforated by two wellbores. The model poroperm properties are conditioned by quantitative empirics from crystalline rock well-log, well-core, well-temperature and well-stimulation data: (i) spatially-correlated porosity attested by well-log power-spectral scaling, $S_\varphi(k) \sim 1/k$ for spatial frequencies 1/km < k < 1/m; (ii) well-core poroperm spatial correlation $\kappa \sim exp(\alpha\varphi)$ with empirical parameter α having ambient values such that $\alpha\underline{\varphi} \sim$ 3-4 for porosity $\underline{\varphi} \sim$ 0.01; (iii) wellbore-centric Peclet number $P_e \equiv r_0 v_0 \underline{\varphi}/D \sim 10$ observed at 1.5km depth for heat advected by isolated naturally-occurring fracture-connectivity structures in basement rock (r_0 = wellbore radius, v_0 = fluid velocity at wellbore, $\underline{\varphi}$ = mean formation porosity, and D = thermal diffusivity of rock-fluid system); (iv) fluid injection flow rates ~ 10L/s at 70-90MPa wellbore pressure; (v) induced microseismicity with spatial correlation scaling function $G(r) \sim 1/r^{1/2}$, 30m < r < 500m, derivable from empirics (i)-(ii). Generation of permeability stimulation fluid pathways constrained by this suite of spatially-correlated rock-fluid interaction empirics is hypothesised in place of non-existent large-scale discrete fractures of standard permeability stimulation scenario.

Aspects of our computational and observational exercise for EGS stimulation of wellbore-pair crystalline rock volumes at 6km depth are (i) the wellbore-centric radius at which interwell-offset joint pressurisation is effective for presently achievable wellbore pressures; (ii) the degree of permeability enhancement achieved with joint wellbore pressurisation; (iii) the relation between near-wellbore permeability enhancement and induced microseismicity. Sustained interwell flow of Peclet number $P_e \sim 5$ along substantial portions of km-length wellbore-pairs appears feasible for commercial heat supply to the Otaniemi district heating plant. Present results imply

a formidable barrier to $P_e \sim 75$ wellbore-to-wellbore heat extraction for electrical power once commonly considered as an achievable EGS target.

2. GETTING BEYOND CRUSTAL FRACTURES AS DISCONTINUITIES IN AN ELASTIC CONTINUUM

The longstanding approach to rock fracture processes takes crustal rock as an elastic continuum in which fracture generation proceeds via a stress singularity at the fracture tip [17]. In the elastic continuum approach to crustal fracture mechanics, fluids have a subordinate role restricted to modifying the micromechanics of the crack tip and introducing a fluid-diffusion time scale on the fracture generation process [18].

Two 1957 papers by Hubbert exemplified, even codified, the elastic continuum conceptual framework for crustal rock-fluid interaction. In a centennial celebration of Darcy's Law [19], rock was taken to be an effectively homogeneous poroelastic medium. Water content was largely a passive partner that flowed as permitted by sets of spatially-uncorrelated random fracture discontinuities in an otherwise homogeneous elastic continuum. A second paper described the hydrofracture stimulation of reservoir rock in terms of regional stress orientation by which Griffiths cracks in an elastic continuum open against the minimum principal stress and propagate indefinitely along the direction of maximum principal stress [20]. Bear developed the Hubbert theme by introducing the REV – the representative elementary volume – of crustal rock above which scale all volumes within a given geological formation had very similar mean flow properties [21].

The Hubbert-Bear elastic continuum view of rock and fluids in rock has, however, nothing compelling to say in response to the vast array of well-log, well-core, and well-production empirics that explicitly contradict its twin assumptions of spatially uncorrelated fractures and fluid passivity:

(I) Long-range macro-scale collective behaviour in crustal rock is attested by the ''1/*k*-noise'' power-law scaling nature of well-log Fourier power-spectra, $S(k) \propto 1/k^{\beta}$, $\beta \sim 1$, $1/\text{cm} < k < 1/\text{km}$ [22]. This five-decade power-law scaling feature applies in particular to porosity measured by neutron scattering in reservoir and basement rock from 1-6km depths. The concept of spatial heterogeneity codified by Hubbert requires with mathematical exactitude that well-log spectra have ''white noise' power-spectrum, $S(k) \propto 1/k^0 \sim const.$

(II) An intimate relation between rock's solid and fluid components is attested by the well-core spatial correlation systematics of spatially varying porosity φ and permeability κ, $\delta \log \kappa \sim \alpha \delta \varphi$ [23-25]. Rock permeability on this evidence is a physical feature of fracture-connectivity between spatially-correlated porosity structures at all scales throughout a crustal volume. The empirical scaling constant α in the well-core poroperm spatial correlation is observed to obey the condition $\alpha \underline{\varphi} \sim 3\text{-}4$ for two decades of mean porosity, $0.3\% < \underline{\varphi} < 30\%$, spanning the basement-to-reservoir geology spectrum [26].

(III) The empirical condition $\alpha \underline{\varphi} \sim 3\text{-}4$ guarantees lognormal distributions for the integrated poroperm relation $\kappa \sim \kappa_0 \exp(\alpha \varphi)$ describing well-productivity for crustal-scale fluid flow systems. Lognormal well-productivity distributions are observed everywhere for groundwater aquifers, conventional and unconventional hydrocarbon reservoirs, convective geothermal systems, and mineral deposition abundances in fossil flow systems [27-30]. Lognormal distributions thus fundamentally contradict the Hubbert-Bear spatial averaging tenet and its consequent continuum approximation.

As replacement for rock-as-elastic-continuum, rock-fluid empirics put a specific 'atom' of grain-scale fluid-rock interaction energetics at the heart of rock fracture mechanics. The 'atom' of rock-fluid interaction has two energy states depending on whether pore fluids can or cannot pass through a grain locus. If a pore fluid can pass to a neighbour pore, the rock-fluid medium at the pore site has elastic interaction energy ε. If pore fluid at the pore site cannot pass to a neighbour pore, the site energy has value $\varepsilon' \neq \varepsilon$. In these circumstances, rock-fluid interaction and rock fracture mechanics reduces to an exercise in 2D-3D ''Ising model'' macro-state thermodynamics as an ensemble of fluid-rock 'atomic' microstates of binary site energy ε or ε' [26].

It is mathematically established for 2D-3D Ising systems that the 2nd law of thermodynamics guarantees the existence of a system 'critical energy' state in which micro-scale elements exhibit long-range macro-scale collective behaviour. Such collective behaviour is observed in rock-fluid interaction empirics. Well-studied examples of long-range collective behaviour of otherwise short-range 'atomic' binary-state interactions are the critical point of water [31], ferromagnetism in iron atoms at the Curie temperature [32], and critical opalescence for binary fluids at a characteristic temperature and pressure [33]. The long-range development of binary-state rock-fluid interactions turn rock from the essentially featureless quasi-homogeneous Hubbert-Bear elastic continuum with incidental fluids into a poroelastic medium with macroscopic fracture-connectivity structures inherently coupled to pore fluids. In addition to above noted rock-fluid interaction empirics, these spatially-correlated poroelastic flow heterogeneities scatter seismic waves propagating in the upper crust to form the signature seismic coda waves [34]. Seismic coda waves in the crust are directly analogous to cloudiness due to light scattering in binary fluids at critical opalescence

Focusing on evidence for individual crustal fractures per se, we note that outcrop evidence which is generally taken to imply the existence of large-scale crustal fracture discontinuities at depth is more precisely evidence for the vanishing of crustal stress at a free surface. No compelling physical logic for direction observations supports fractures-as-elastic-continuum-discontinuities persisting to significant crustal depths as is often projected [35-36]. Considering direct evidence for open fractures in well-log data, there is singular absence of evidence in FMI micro-resistivity data for discrete open-fracture conductivity highs that might be expected signal large-scale open fractures. The properties of FMI logs illustrated in Appendix 2 include 1/*k*-spectral-scaling distributions of resistivity with occasional occurrence of discrete conductivity lows that are logically attributable to fossilised flow systems filled with calcite or silica [26].

In light of the range of negative evidence for crustal fractures as discontinuities in a quasi-uniform elastic continuum, and the positive evidence for crustal fractures as spatially-correlated distributions of grain-scale fracture-continuity as summarised in crustal fluid-

rock interaction empirics (I)-(III), we look in detail at how pressurised wellbore fluids can interact with the ambient fluid content of tight crystalline rock to stimulate permeability at depth in the Fennoscandian basement [37-38].

3. MODELLING WELLBORE-CENTRIC FLUID FLOW WITH FRACTURE-CONNECTIVITY EMPIRICS (I)-(III)

Steady-state rock-fluid interactions and related flow stimulation may be modelled for wellbore-centric flow geometry by embedding cylindrical pressure boundary surfaces in a 3D number field representing porosity spatially varying $0 < \varphi_{min} < \varphi(x,y) < \varphi_{max} < 1$. As illustrated in Fig 1, the porosity field spatial variations have the empiric (I) spectral scaling property $S_\varphi(k) \propto 1/k$. Fluids under pressure in the annular volume flow according to Darcy permeability $\kappa(x,y) \sim \kappa_0 \exp(\alpha\varphi(x,y))$ given by empiric (II) with empirical constant α fixed by well-core poroperm data as guided in empiric (III). While the numerical porosity and permeability number fields have clear and familiar physical interpretations, the role of parameter α emerges only from crustal empirics.

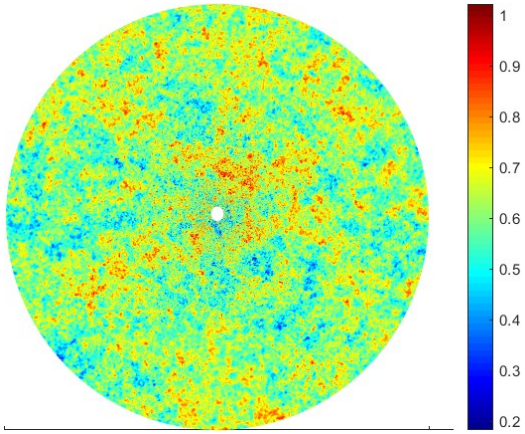

Figure 1: Wellbore-centric crustal section of spatially-correlated porosity fluctuations normally distributed between 0.2% and 1% with mean $\underline{\varphi} \sim 0.6\%$. A linear sequence of porosity values recorded at approximately 500 grid points along a radius R has a power-spectrum $S_\varphi(k)$ that scales inversely with spatial frequency in range $1/R < k < 250/R$, $S_\varphi(k) \sim 1/k$ set by crustal fluid-rock interaction empiric (I). The associated permeability of the crustal section is $\kappa \sim \kappa_0 \exp(\alpha\varphi)$, with empirical condition $\alpha\underline{\varphi} \sim 3$-4 setting fracture-connectivity parameter $\alpha \sim 600$.

We take the Fig 1 canonical spatial correlation nature of crustal rock porosity to represent a 2D planar crustal section of nominal 20-meter radius with 1-meter unit thickness penetrated by a central wellbore. The empirical constant α, fixed by $\alpha\underline{\varphi} \sim 3$-4 for mean porosity $\underline{\varphi}$, determines the degree to which porosity-clustering at all scales enables fluid flow via grain-scale fracture connectivity [26].

Macroscope flow simulations are finite-element solutions to the equations of conservation for mass and heat energy applied to the Fig 1 geometry. Flow boundary conditions are related to controlled quasi-steady-state injection and production of fluids at a wellbore or a wellbore-doublet in low-porosity/low-permeability basement rock at 6km depth [37]. Wellbore heat energy boundary conditions are either a fixed temperature or Newton cooling, in which heat energy flux at the interface is proportional to temperature at the interface. Volumetric fluid velocity V [m^3/s] in a wellbore section of radius r_0 and nominal length ℓ in a rock volume of mean porosity $\underline{\varphi}$ is given by $V = 2\pi r_0 \underline{\varphi} v_0$ for Darcy flow velocity v_0 at the wellbore wall at radius r_0. Heat energy fluid transport along a wellbore Q [W] is given by volumetric flow rate, volumetric heat capacity $\rho C \sim 4.28$MJ/m^3·°C, and fluid temperature T, $Q = V\rho CT$. Observed stimulation activity pressure and flow data give wellbore boundary condition control for fluids from which to compute wellbore heat extraction rates Q [37]. Quasi-steady-state wellbore axial temperature variations give control on inner wellbore heat exchange proportionality constant [38].

Darcy's law of fluid flow in crustal rock relates the fluid pressure gradient $\nabla P(x,y)$ [Pa/m] to the speed $\boldsymbol{v}(x,y)$ [m/s] at which a parcel of fluid flows within rocks granular framework,

$$\boldsymbol{v} = \kappa/\mu \, \nabla P; \tag{1}$$

the Darcy's law proportionality coefficient κ/μ is given by the dynamic viscosity of the fluid μ [Pa·s] and spatially variable rock permeability $\kappa(x,y)$ [m^2]. Bulk fluid flow and heat transport within a rock volume of mean porosity $\underline{\varphi}$ is the product of Darcy velocity and mean porosity, $\underline{\varphi}v$.

Conservation of mass requires that steady-state Darcy flow velocity has vanishing divergence, $\nabla\cdot\boldsymbol{v} = 0$, yielding the defining flow equation for finite-element solvers,

$$\nabla\cdot(\kappa(x,y)\nabla P(x,y)) = 0. \tag{2}$$

Darcy flow is controlled by appropriate fluid pressure boundary conditions in the Fig 1 crustal section.

For Darcy fluid flow transporting heat through a crustal medium of mean porosity $\underline{\varphi}$, the combined conduction and advection of heat energy is given in terms of temperature field $T(x,y)$,

$$\mathbf{q} = K\nabla T(x,y) - \rho C\underline{\varphi}\boldsymbol{v}(x,y)T(x,y), \tag{3}$$

K = Fourier's coefficient of thermal conductivity for rock.

Conservation of steady-state conductive and advective heat energy, $\nabla\cdot\boldsymbol{q} = 0$, couples the spatially-variable temperature field $T(x,y)$ to the spatially-variable Darcy fluid velocity flow field $\boldsymbol{v}(x,y)$ for the given crustal temperature and fluid pressure boundary conditions. This coupling leads to the defining steady-state equation for a nonlinear finite-element solver,

$$\nabla\cdot\nabla T(x,y) = \underline{\varphi}/D\ \boldsymbol{v}(x,y)\cdot\nabla T(x,y). \tag{4}$$

In the approximation that Darcy fluid flow velocity is radial, $\boldsymbol{v}(r) \sim r_0 v_0/r$, in wellbore-centric radial domain $r_0 \le r \le r_1$, the conservation of heat energy condition,

$$\nabla^2 T(r) = 1/D\ \underline{\varphi}\boldsymbol{v}(r)\cdot\nabla T(r), \tag{5}$$

can be expressed analytically. For radial component divergence operator $\nabla\cdot\mathbf{A}(r) = 1/r\ \partial_r(rA_r)$, (5) becomes

$$\partial_r{}^2 T(r) + (1 - P_e)/r\ \partial_r T(r) = 0, \tag{6}$$

for $P_e = r_0\underline{\varphi}v_0/\mathrm{D}$ the Peclet number for wellbore-centric flow. The analytic solution to (6) is

$$T(r) = T_0 + (T_1 - T_0)\cdot((r/r_0)^{Pe} - 1) / ((r_1/r_0)^{Pe} - 1). \tag{7}$$

Wellbore-centric steady-state heat advection expression (7) closely parallels the Bredehoeft & Papadopulos [39] expression for steady-state heat advective fluid transport normal to layers in a planar crustal medium,

$$T(z) = T_0 + (T_L - T_0)\cdot(e^{\beta z/L} - 1)/(e^{\beta} - 1), \tag{8}$$

with planar Peclet number $\beta \equiv v_0\rho CL/K$ for layer thickness L with thermal constants $\rho C/K = 1/D$ traversed by a fluid front moving at velocity v_0. Appendix 1 fixes the equivalent planar-flow Peclet number for laminar fluid flow in planar fracture-discontinuities in an otherwise uniform crust.

The key rock-fluid interaction physical process affecting macroscale flow in crustal rock is fracture-connectivity governed by the scale-independent fracture-connectivity parameter α defined by the empirical relation $\kappa(x,y) \sim \kappa_0\ exp(\alpha\varphi(x,y))$. For a given normally distributed porosity field $\varphi_{min} < \varphi(x,y) < \varphi_{max}$ with mean $\underline{\varphi} \sim (\varphi_{min} + \varphi_{max})/2$, the associated permeability field has values of α such that $\alpha\underline{\varphi} \sim$ 3-4 [26]. This empirical condition mathematically guarantees the permeability distribution to be lognormal in accord with essentially universal field evidence that well production of crustal fluids – groundwater, conventional and unconventional hydrocarbons, geothermal fluids, mineral deposition of fossil flow systems – is everywhere lognormal [27-30]. The empiric $\alpha\underline{\varphi} \sim$ 3-4 is valid across the range of crustal porosities $0.003 < \varphi < 0.3$ spanning the basement-to-reservoir rock spectrum. For permeability measured in units of Darcy $\equiv 10^{-12}$ m^2, the corresponding 7-to-8 decadal range of permeabilities is 10^{-7} Darcy $< \kappa <$ 10 Darcy. Crustal permeability is thus controlled by the degree of fracture-connectivity at all scales through the parameter α.

The phenomenology of parameter α -- observed for all fluids and observed across the complete range of crustal porosities -- implies that the physical process by which the observed crustal state is naturally achieved is likely to be open to artificial stimulation. Increasing the value of α for a given crustal volume of porosity $\varphi_{min} < \varphi(x,y) < \varphi_{max}$ is a natural and effective way to increase permeability within the crustal volume.

Fig 2 illustrates the role of α in converting normal distributions of spatially-correlated porosity into lognormal distributions of fracture-connectivity permeability. As seen in Fig 2 top-left panel, small values of α yield normally distributed permeability. This follows mathematically for small values of the exponential argument x, the exponential function depends primarily on the linear term, $exp(x) \sim x + x^2/2! + x^3/3! + x^4/4! + \ldots\ldots$ For larger values of α permeability becomes an increasingly skewed lognormal distribution as seen in the remaining panels of Fig 2.

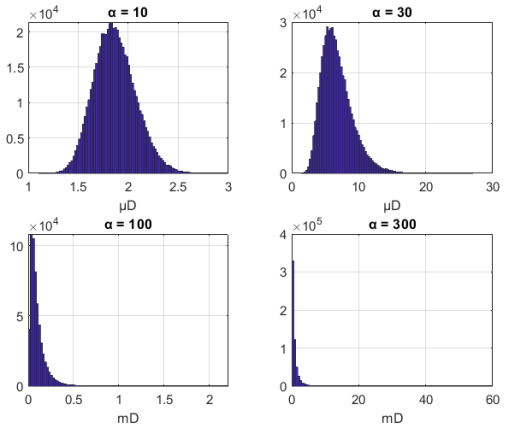

Figure 2: Frequency distributions of permeability, $\kappa \sim \exp(\alpha\varphi)$, for Fig 1 porosity distribution φ as a function of fracture-connectivity parameter α. For low values of α, shown in the upper panels, permeability is small and normally distributed, $\kappa \sim \exp(\alpha\varphi) \sim \alpha\varphi$. For high values of α, shown in the lower panels, permeability is large and lognormally distributed. The small number of spatially-correlated high-permeability fracture-connectivity pathways dominate the crustal section flow structure [26].

The Fig 2 progression of increasing permeability for increasing α is a statement that for any degree of crustal porosity φ, the key physical rock-fluid interaction property is the degree to which fluid-bearing pores are connected. The generic/ambient crust empirical condition αφ ~ 3-4 indicates that α is an active parameter that measures the degree to which pore-interconnectivity is maintained through the large range of crustal compaction processes that reduce porosity and permeability. As porosity falls due to compaction, pore-interconnectivity rises to keep crustal fluids mobile. As a means to increase permeability through fluid injection at crustal depths, it is natural to focus on the mechanics of increasing pore-connectivity rather than increasing porosity. Increasing porosity at depth requires substantial energy. Increasing effective pore-connectivity through reactivating fossilised flow-connectivity pathways is likely to be significantly more energy efficient.

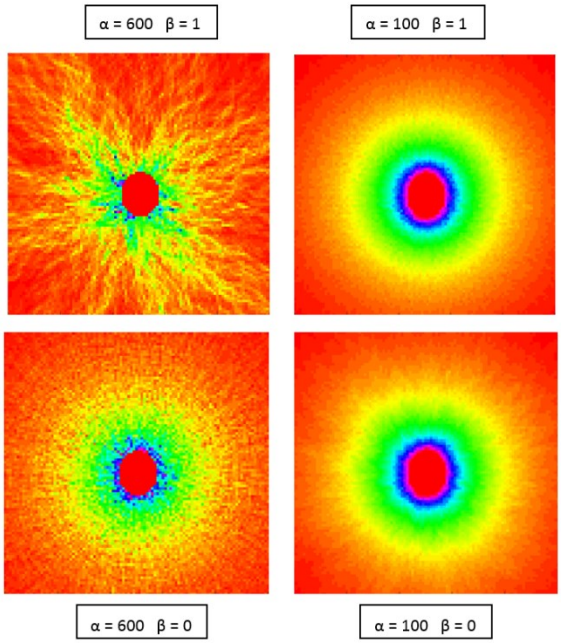

Figure 3: The high degree of fracture-connectivity creating filamentary crustal fluid flow paths away from a wellbore is seen in the upper left panel for porosity spatial-correlation parameter β = 1 and fracture-connectivity parameter α = 600. For uncorrelated porosity β = 0 and/or small α = 100, fluid flow tends to be azimuthally homogeneous. The upper-left β = 1 α = 600 spatially erratic fracture-connectivity flow structures replicate crustal flow in deep basement rock.

The Fig 3 upper left panel for α = 600 and β = 1 shows the extent by which fracture-connectivity controls fluid flow through crustal rock volumes from high porosity aquifer/reservoir geology to low porosity crystalline basement geology. The remaining three panels show fluid flow distributions that are widely accepted as characteristic of crustal flow, but for which there is no supporting rock physical evidence. Very few if any well-log fluctuation sequences give white-noise power spectra, β = 0, and very few if any reservoir well-core sequences give evidence for α << 20 (recalling that α ~ 20 for reservoir rock for porosity range .1 < φ < .3 is equivalent to α ~ 600 for basement rock for porosity range .003 < φ < .01 [26]).

The spatial clustering of Fig 1 porosity, the permeability distributions of Fig 2, and the Fig 3 filamentary fluid flow structures arising from empirical parameters α = 600 and β = 1 in low porosity basement rock collectively illustrate how far the spatial-correlation effects of actual fluid flow differ from the Hubbert/Bear white noise random fluctuations that underpins the elastic continuum hypothesis for crustal rock. We also note that rock-fluid interaction parameters α = 600 and β = 1 are consistent with induced microseismicity spatial correlation function $G(r) \sim 1/r^{1/2}$ at scales r ~ 30m to r ~ 500m [40]. Crustal flow distributions for the remaining parameter options of Figs 2-3 do not support the observed microseismicity spatial correlation function. In consequence, we move beyond the continuum fracture-mechanics as a means for EGS stimulation, and focus instead on the upper left panel of Fig 3 as guide to how wellbore fluids interact with crustal rock via pre-existing fracture-connectivity structures at all scales. Our key physical property in our rock-fluid interaction is fracture-connectivity parameter α: increasing α increases fluid flow.

4. STIMULATING INTERWELL PERMEABILITY TO ENHANCE FLUID PATHWAYS FOR EGS DOUBLETS

On the basis of our discussion of the empirical fracture-connectivity parameter α, we simulate using wellbore fluid pressure to increase fluid flow between injector and producer wellbores. The model ambient flow properties of crustal section are fixed by the spatially-correlated ambient poroperm transmissivity illustrated in Figs 1-3 for a fixed value of α. As in the 2018 Finnish basement wellbore stimulation programme [37], simply injecting fluid into an ambient crustal section sends the wellbore fluid into the crust without adequate means to return to the surface. Engineering/enhancing interwell permeability creates wellbore-to-wellbore fluid pathways to allow injected fluid to perform the heat extraction task previously assumed to proceed via large-scale planar hydrofractures. With stimulated permeability between the injector and producer, injected surface-temperature fluids preferentially flow into the permeability-stimulated interwell zone. Traveling through interwell volume, the fluid extracts heat energy in the course of reaching the production well with minimal fluid loss to the crust.

The stimulation mechanics proceed over 6 steps illustrated in Figs 4-9:

(i) Generate a Fig 1 model ambient crustal section with distributions of Fig 3 spatially-correlated porosity and permeability fracture-connectivity pathways within a crustal volume of uniform α enclosing an injector and a producer wellbore;
(ii) Solve conservation of fluid mass Eq (2) for simultaneously pressurised wellbores exerting maximum fluid pressure in the interwell crustal section to increase fracture-connectivity parameter α between the injector and producer (Fig 4 left);
(iii) Use a normalised dual-wellbore pressure distribution as weighting function to increase α in proportion to fluid pressure across the crustal section (Fig 5);
(iv) Solve Eq (2) for the crustal section fluid velocity field $\boldsymbol{v}(x,y)$ generated by over-pressure at the injector and under-pressure at the producer (Fig 4 right); Fig 6 contrasts the fluid velocity distribution for ambient permeability (left) and stimulated permeability (right);
(v) Solve conservation of energy heat transport condition Eq (4) to give steady-state temperature distribution for fixed wellbore temperature at the injector and Newton cooling condition at producer; Fig 7 (left, right) shows the steady-state temperature distributions for ambient and stimulated crustal section;
(vi) Use volumetric fluid flow $V = 2\pi r_0 v_0 \varphi \ell$ [m^3/s] in/out of the wellbores to give the steady-state wellbore advective heat flow per meter (ℓ = 1m) of section thickness, $Q = V\rho CT$[W/m] for injector and producer wellbores in the ambient and stimulated crust (Fig 8); also estimate the Peclet number $P_e \equiv r_0 v_0 \underline{\varphi}/D$ for the various flow conditions, where r_0 = wellbore radius, v_0 = fluid velocity at wellbore interface, $\underline{\varphi}$ = mean formation porosity, and D = thermal diffusivity of rock-fluid system (Fig 9).

On the basis of our discussion of the empirical fracture-connectivity parameter α, we simulate using wellbore fluid pressure to increase fluid flow between injector and producer wellbores. The model ambient flow properties of crustal section are fixed by the spatially-correlated ambient poroperm transmissivity illustrated in Figs 1-3 for a fixed value of α. As in the 2018 Finnish basement wellbore stimulation programme [37], simply injecting fluid into an ambient crustal section sends the wellbore fluid into the crust without adequate means to return to the surface. Engineering/enhancing interwell permeability creates wellbore-to-wellbore fluid pathways to allow injected fluid to perform the heat extraction task previously assumed to proceed via large-scale planar hydrofractures. With stimulated permeability between the injector and producer, injected surface-temperature fluids preferentially flow into the permeability-stimulated interwell zone. Traveling through interwell volume, the fluid extracts heat energy in the course of reaching the production well with minimal fluid loss to the crust.

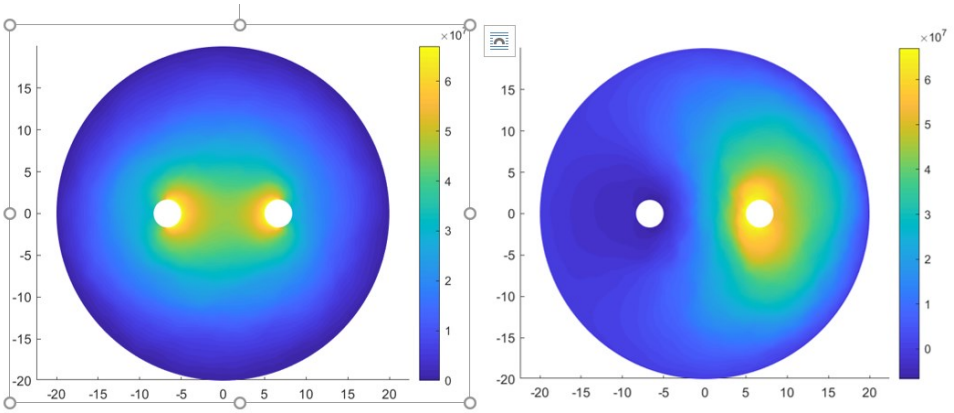

Figure 4: Steady-state crustal section pressure fields [Pa] relative to ambient pressure for jointly stimulated wellbore pair (left) and for circulating fluid from injector to producer (right).

Fig 4 illustrates the steady-state crustal section pressure field generated by wellbore pressurisation. When injector and producer wellbores are jointly pressurised (left), the highest pressures focus on interwell crustal section where the greatest stimulation occurs. When the producer wellbore pressure is reduced below ambient pressure (right), fluid flows from the injector to the producer.

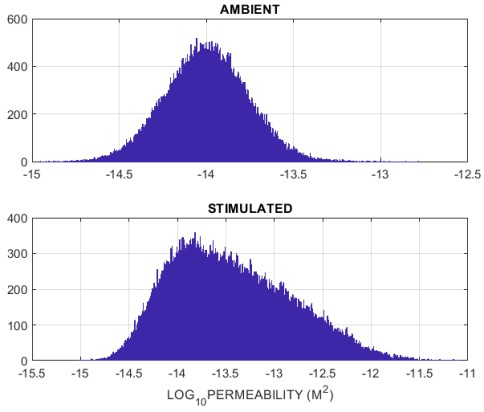

Figure 5: Distribution of ambient permeability (top) and stimulated permeability (below).

The ambient crustal permeability is lognormally distributed (upper) according to the well-core attested poroperm empirical relation $\kappa(x,y) \sim \kappa_0 \, exp(\alpha\varphi(x,y))$ displayed in Fig 5 in the form $\log_{10}(\kappa(x,y)) \sim \alpha\varphi(x,y)$ where the porosity distribution is normally distributed. The median permeability, $\kappa_0 \sim 10^{-14}$ m^2, is representative of crustal rock at the 1-100m scale range (Appendix 2). The process of stimulating the interwell crustal section is hypothesised to increase the local grain-scale fracture-connectivity parameter $\alpha \rightarrow \alpha + W(x,y)\alpha$, where $W(x,y)$ is a normalised weighting function taken to be proportional to the stimulation pressure at section location (x,y). Because of enhanced fracture-connectivity at interwell locations, fluid can pass more easily from injector to producer along reactivated filamentary fracture-connectivity pathways. Fig 6 compares injector-to-producer flow in the ambient crust (left) and the stimulated crust (right). Flow in the stimulated section is both greater and focused on injector-to-producer pathways rather than losing fluid to the ambient crust.

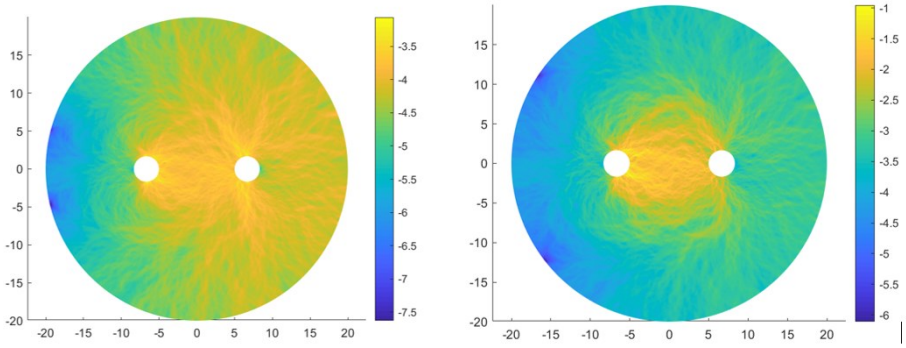

Figure 6: Filamentary fluid-flow pathways for ambient (left) and stimulated (right) injection-producer in wellbore interval. Ambient permeability distribution loses significant injected fluids to ambient crust, while stimulated permeability distribution focuses injected fluid pathways to producer. Peak fluid velocities in/out of wellbores are ~ 10^{-3} m/s for ambient permeability and ~ 10^{-1} m/s for stimulated permeability. Velocity magnitudes given in logarithm scale.

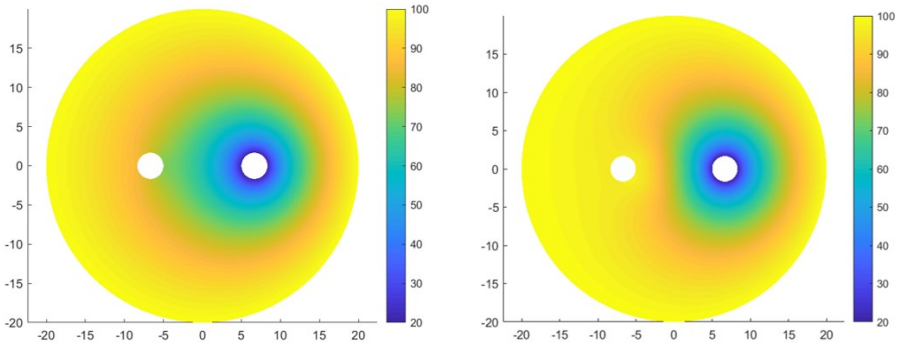

Figure 7: Steady-state temperature fields for ambient advective heat flow (left) and stimulated advective heat flow (right). The injection well temperature is fixed at 20°C. The production well boundary condition is Newton cooling heat flux. Heat extraction rate is smaller for ambient permeability than for stimulated permeability. The difference in heat extraction between stimulated flow and unstimulated flow is a measure of the EGS process.

The steady-state flow solutions to conservation of heat energy equation (4) are shown in Fig 7 for the ambient crustal section (left) and stimulated crustal section (right). These solutions balance the heat lost to the section from the producer against the heat brought to the crustal section by the injector, and by thermal conduction and thermal advection from the section boundary. The effect of permeability stimulating the interwell crustal section is to draw heat from the crustal section into the neighbourhood of the producer. Because of the greater rate of fluid flow in the stimulated section, the stimulated section reaches its steady-state faster than does the ambient crustal section. Because of the stimulation pathways, the mean steady-state temperature of the stimulated crustal section is greater than the mean steady-state temperature of the ambient crustal section.

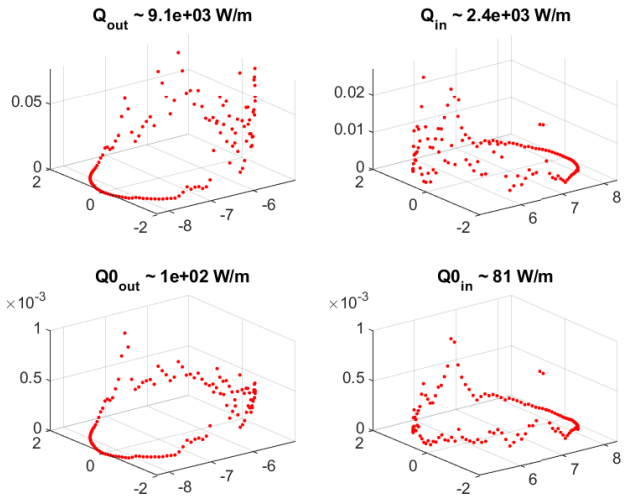

Fig 8 – Azimuthal distributions of wellbore heat transport in W per meter thickness of crustal section. Upper plots are for stimulated sections and lower plots are for unstimulated sections; left plots are for production well, and right plots are for injector well. Azimuthal variation in heat flux around the wellbore is due to fluctuations in permeability distribution in the crustal section.

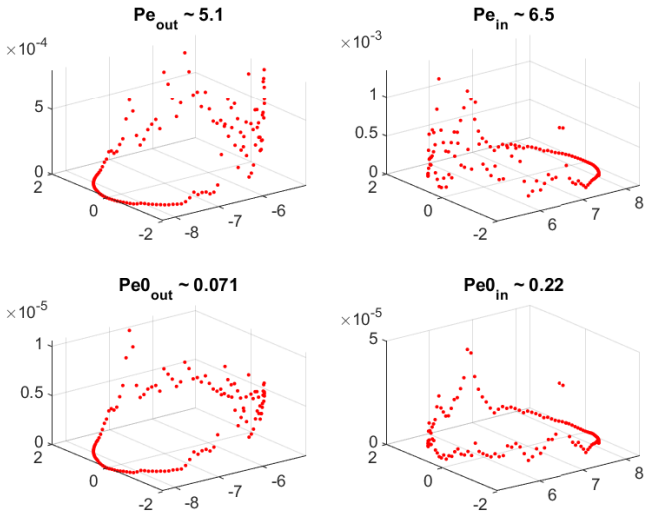

Figure 9: Azimuthal distributions of wellbore fluid velocity in m/s at wellbore boundaries. Upper plots are for stimulated sections and lower plots are for unstimulated sections; left plots are for production well, and right plots are for injector well. Peclet numbers indicate that unstimulated sections are essentially non-advective ($P_e << 1$) while stimulated sections are advective ($P_e > 1$). Azimuthal variation of fluid velocity around the wellbore is due to fluctuations in permeability distribution in the crustal section.

Figs 8-9 show the steady-state heat flux and fluid flux conditions at the injector and producer wellbores for both stimulated and ambient crustal sections. Of prime interest is the producer heat flux for the stimulated crustal section (Fig 8 upper left) and the Peclet numbers for the stimulated sections (Fig 9 upper left, right). For the large diameter wellbore shown if Figs 4-9, the producer heat flux is 9kW per meter of crustal section thickness, or 9MW per km of stimulated well. The associated Peclet numbers for this model flow are $P_e \sim 5$. This level of advective heat transport is comparable to the naturally-occurring heat transport observed in granites at 1.5 km depth at the Otaniemi drill site.

5. THE EFFECT OF WELLBORE RADIUS ON STIMULATING INTERWELL PERMEABILITY

Figs 4-9 illustrate the hypothetical stimulation process for a model with large wellbore radii. Fig 10 (left) illustrates the equivalent model computation for wellbores that are 10 times smaller. It is seen that the producer heat flux output is itself 10 times smaller than that of the Figs 4-9 model, and that the Peclet number is 5 times smaller. The same scaling result is shown in Fig 10 (right) for intermediate wellbore radii differing by factor 3 from the two previous models. Fig 11 summarises this scaling relation for six parameters model parameters at five wellbore radii between 0.16m and 1.6m.

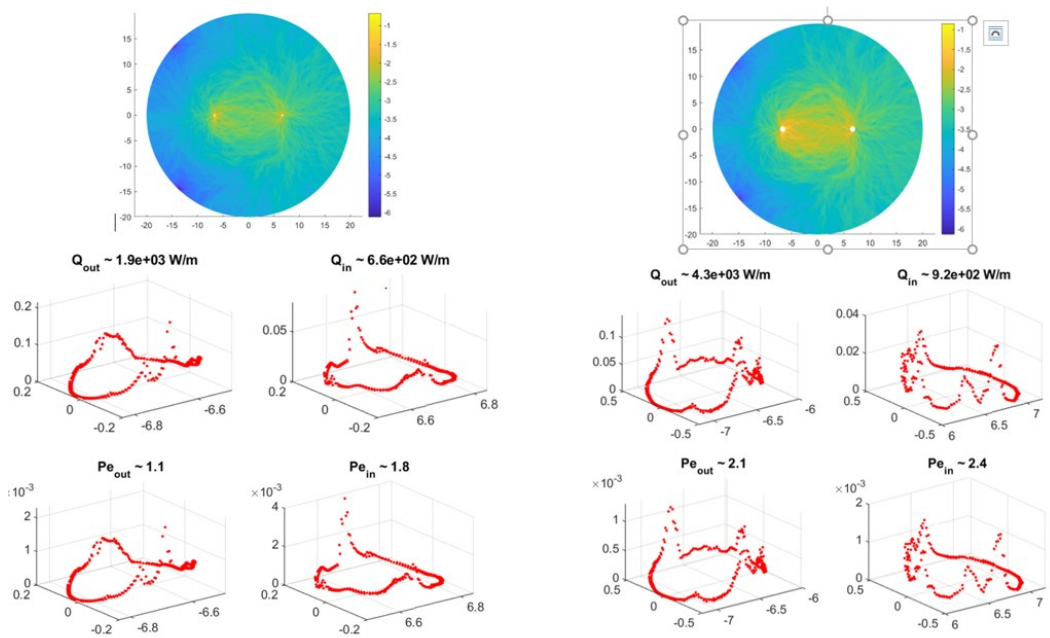

Figure 10: (Lef t) Reprise of Figs 6,8,9 for small diameter wellbores in stimulated rock section. (Right) Intermediate diameter wellbores in stimulated rock section. Upper plot velocity magnitudes are on a logarithmic scale; lower plot heat fluxes and fluid velocities are on a linear scale.

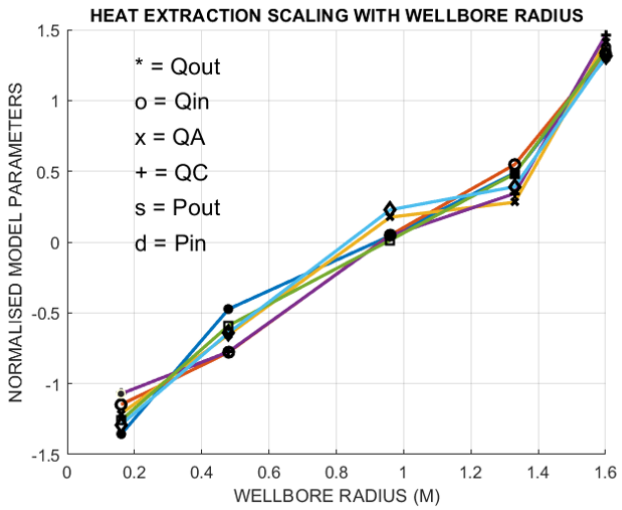

Figure 11: Scaling of normalised stimulation model parameters with wellbore radius. Qout = producer heat flux; Qin = injector heat flux; QA = heat flux advected across model boundary; QC = heat flux conducted across model boundary; Pout = producer Peclet number; Pin = injector Peclet number. Fluctuations in parameter magnitudes for different wellbore sizes reflect statistical variation within the model porosity and permeability distributions.

The stimulation effect dependence on wellbore radius is due to wellbore-fluid-induced pressure decrease with distance from the center. From Eq (2) for constant permeability, $\nabla\cdot\nabla P(r) = \nabla^2 P(r) = \partial_r(r\partial_r P(r))$, the crustal pressure field declines with radius, $P(r)=P_0 + (P_1-P_0)log(r_0/r)/log(r_0/r_1)$, in the annulus $r_0 < r < r_1$. If, however, the effect of near-wellbore stimulation is to greatly increase the permeability of the near-wellbore crust, the effective interior radius r_0 of the pressure field increases. It thus becomes of great interest to understand, and perhaps manipulate, the stimulation mechanics of wellbore pressurisation in the near vicinity of the wellbore. The greater the effective wellbore radius, the greater the permeability stimulation and the greater the producer heat flux.

6. SUMMARY/CONCLUSIONS

Slow, steady wellbore pressurisation of 200m intervals of open wellbore in crystalline basement rock at 6km depth has reactivated fossilised spatially-correlated fracture-connectivity fluid pathways in the surrounding crust. By entering the crust via pre-existing fracture-connectivity pathway (rather than creating fresh large-scale discrete quasi-planar fractures), the injected fluids induced thousands of spatially-correlated microseismic slip events in a cylindrical volume about the stimulation wellbore [37]. The observed two-point spatial correlation function for the induced seismicity is precisely what is expected for reactivation of pre-existing spatially-correlated fluid flow paths [40]. The absence of microseismicity associated with large-scale quasi-planar fracture surfaces to connect the injector well to a putative producer well requires that alternative stimulation mechanics must be found.

To this end, we have invoked the highly-attested essentially universal evidence that high degree of spatial correlation phenomenology connects crustal fluids to crustal rock at all scales from mm to km across a wide range of geological settings given as empirics (I)-(III). In sedimentary rock formations, the rock-fluid interaction remains active, maintaining a fixed relation between porosity and permeability, $\kappa(x,y) \sim \kappa_0 \exp(\alpha\varphi(x,y))$, with the empirical parameter constrained by the condition $\alpha\underline{\varphi} \sim 3\text{-}4$, where $\underline{\varphi}$ is the mean formation porosity typically in the range $0.1 < \underline{\varphi} < 0.3$. In crystalline rock, subjected to metamorphic pressures and temperature, the previously active rock-fluid interaction is fossilised by silica and calcite. However, even as the mean formation porosity declines to $0.001 < \underline{\varphi} < .01$, the condition $\alpha\underline{\varphi} \sim 3\text{-}4$ remains intact during the fossilisation process. The empirical parameter thus continues to play a role in the permeability of basement rock.

While it is manifestly difficult to increase porosity in basement rock – all porosity increases have to do work against the large confining stresses -- it is not necessarily difficult to increase fracture-connectivity in basement rock. Accordingly, we have approached EGS permeability stimulation in terms of high-pressure wellbore fluid reactivating fossilised flow-structure connectivity, and in doing so, locally increasing the value of the empirical parameter α. Our simulations can generate reasonable permeability increases in the context of reasonable physical parameters for basement rock.

Because our fracture-connectivity flow mechanics provide intimate fluid contact with the rock heat store, the present heat exchange model is potentially more efficient than the traditional crustal slab-cooling heat exchanger [1-9]. At the same time, wellbore-centric fluid pressure fields that drive stimulation fluids into the crustal fracture-connectivity structures decay logarithmically with radial offset from the wellbore, and plausibly limiting the effective stimulation radius.

Looking forward to the dual-wellbore EGS stimulation data acquired at the Otaniemi site, we can our stimulation mechanics to consider the following points for more detailed computation:

(i) Feasible wellbore effective radii at which interwell-offset joint pressurisation is effective for presently achievable wellbore pressures;
(ii) Degree and spatial extent of permeability enhancement achieved with joint wellbore pressurisation;
(iii) Use of near-wellbore seismic array sensors to identify axial and radial spatial relations that connect permeability enhancement with induced microseismicity;
(iv) Potential induced seismicity concentration in immediate vicinity of the wellbore indicating creation of a wellbore-centric damage halo to enhance stimulation radius;
(v) Axial temperature fields due to sustained interwell flow of Peclet number $P_e \sim 5$ along portions of the wellbore-pair axis signalling feasible commercial heat supply to the Otaniemi district heating plant.

Present stimulation computation indicates a formidable barrier to $P_e \sim 75$ wellbore-to-wellbore heat extraction for electrical power that was once commonly considered as an achievable EGS target. Interwell offsets required to sustain high Peclet number heat extraction appear to be significantly beyond current technical means. That said, moderate $P_e \sim 5$ wellbore-to-wellbore heat extraction has good prospects for direct use application such as drives the St1 Deep Heat project at Otaniemi, Finland [37].

REFERENCES

[1] Hubbert MK & Willis DG (1957) Mechanics of hydraulic fracturing. *Petrol. Trans. AIME*, 210: 153--166.
[2] Harlow FH & Pracht WE (1972) A Theoretical Study of Geothermal Energy Extraction, *J. Geophys. Res.* 77, 7038-7048.
[3] Gringarten AC, Ramey HJ & Raghaven R (1974) Unsteady-state pressure distributions created by a well with a single infinite-connectivity vertical fracture, *Journal Society of Petroleum Engineers*, Vol 14 (SPE_04051).
[4] Gringarten AC, Witherspoon PA & Ohnishi Y (1975) Theory of Heat Extraction from Fractured Hot Dry Rock, *J. Geophys. Res.* 80, 1120-1124.
[5] Wunder R & Murphy H (1978) Singly and multiply fractured hot dry rock reservoirs, Los Alamos National Laboratory Report, LA-7219-MS, UC-66a, 1-15.
[6] Smith MC (1983) A History of Hot Dry Rock Geothermal Energy Systems, *Journal of Volcanology and Geothermal Research*, 15 1--20 Elsevier Scientific Publishing Company, Amsterdam
[7] Tester J et al. (2006) The future of geothermal energy—Impact of enhanced geothermal systems (EGS) on the United States in the 21st Century; http://mitei.mit.edu/publications/reports-studies/future-geothermal-energy.
[8] Sutter D, Fox DB, Anderson BJ, Koch DL, Von Rohr PF, Tester JW (2011) Recovery in a Model EGS Fractured Reservoir, 36th Workshop on Geothermal Reservoir Engineering, Stanford Geothermal Program Workshop Report SGP-TR-191
[9] Jain C, Vogt C & Clauser C (2015) Maximum potential for geothermal power in Germany based on engineered geothermal systems, *Geothermal Energy* (2015); DOI 10.1186/s40517-015-0033-5.
[10] Hasting M, Albaric J, Oye V, Reid P, Messeiller M, Llanos E, Malin P, Shalev Hogg M, Alvarez M, Miller A, Walter C, Boese C & Voss N (2011) Real-time induced seismicity monitoring during wellbore stimulation, Australian Geothermal Energy Conference; https://www.geothermal-energy.org/pdf/IGAstandard/AGEC/2011/GA20050.pdf
[11] Bendall B, Huddlestone-Holmes C & Goldstein B (2013) The current status of geothermal projects in Australia - a national review proceedings, 38th Workshop on Geothermal Reservoir Engineering Stanford University, February 11-13, 2013 SGP-TR-198
[12] Bendall B, Hogarth R, Holl H, McMahon A, Larking A & Reid P (2014) Australian experiences in EGS permeability enhancement – A Review of 3 case studies, 39th Workshop Geothermal Reservoir Engineering, Stanford University, SGP-TR-202.
[13] Moeck IS (2014) Catalog of geothermal play types based on geologic controls, *Renewable and Sustainable Energy Reviews 37*, 867–882.
[14] Moeck IS & Beardsmore G (2014) A new 'geothermal play type' catalog: Streamlining exploration decision making, 39th Workshop on Geothermal Reservoir Engineering Stanford University, February 24-26, 2014 SGP-TR-2021
[15] Agemar T, Weber J & Moeck IS (2018) Assessment and Public Reporting of Geothermal Resources in Germany: Review and Outlook, *Energies*, 11, 332; doi:10.3390/en11020332.

[16] Dussel M, Moeck I, Wolfgramm M & Straubinger R (2018) Characterization of a deep fault zone in Upper Jurassic carbonates of the northern alpine_foreland basin for geothermal production (South Germany), 43rd Workshop on Geothermal Reservoir Engineering Stanford University, February 12-14, 2018 SGP-TR-2131.
[17] Rice JR (1968), Mathematical Analysis in the Mechanics of Fracture, *Fracture: An Advanced Treatise* Vol. 2, *Mathematical Fundamentals* (ed. H. Liebowitz) Academic Press, NY; pp. 191-311.
[18] Rice J & Cleary MP (1976) Some Basic Stress Diffusion Solutions for Fluid-Saturated Elastic Porous Media with Compressible Constituents, *Reviews of Geophysics and Space Physics*, 14, No 2, 227-241.
[19] Hubbert MK (1957) Darcy's law and the field equations of the flow of underground fluids, *International Association of Scientific Hydrology, Bulletin*, *2:1*, 23-59; doi: 10.1080/02626665709493062.
[20] Hubbert MK & Willis DG (1957) Mechanics of Hydraulic Fracturing, *Petroleum Transactions, AIME*, Vol. 210, 153-168.
[21] Bear J (1972) *Dynamics of Fluids in Porous Media*, American Elsevier: New York, NY, USA.
[22] Leary PC (2002) Fractures and physical heterogeneity in crustal rock, in *Heterogeneity of the Crust and Upper Mantle – Nature, Scaling and Seismic Properties*, JA Goff & K Holliger eds., Kluwer Academic/Plenum Publishers, New York, 155-186.
[23] Leary PC & Al-Kindy F (2002) Power-law scaling of spatially correlated porosity and log(permeability) sequences from northcentral North Sea Brae oilfield well core, *Geophysical Journal International 148*, 426-442.
[24] Leary P, Malin P & Niemi R (2017) Finite-Element Modelling of Wellbore-Observed Fracture-Borne Heat Advection – Application to EGS Stimulation in Basement Rock, 41st Workshop Geothermal Reservoir Engineering, Stanford University, February 13-15, SGP-TR-212.
[25] Leary P, Malin P & Niemi R (2017) Fluid flow & heat transport computation for power-law scaling poroperm media, *Geofluids*, Volume 2017, https://doi.org/10.1155/2017/9687325
[26] Leary P, Malin P, Saarno T & Kukkonen I (2018) αφ ~ αφ crit – Basement rock EGS as extension of reservoir rock flow processes, 43rd Workshop on Geothermal Reservoir Engineering Stanford University, Stanford, California, February 12-14, 2018 SGP-TR-213.
[27] Malin P, Leary P, Shalev E, Rugis J, Valles B, Boese C, Andrews J & Geiser P (2015) Flow lognormality and spatial correlation in crustal reservoirs: II – Where-to-drill guidance via acoustic/seismic imaging, WGC2015, 19-24 April, Melbourne AU.
[28] Gustafson G (2002) Strategies for groundwater prospecting in hard rocks: a probabilistic approach, *Norges geologiske undersøkelse Bulletin,* vol. 439, pp. 21–25;
[29] Banks D, Gundersen P, Gustafson G, Makela J & Morland G (2010) Regional similarities in the distributions of well yield from crystalline rocks in Fennoscandia, *Norges geologiske undersøkelse Bulletin*, vol. 450, pp. 33–47;
[30] Krige DG (1981) Lognormal de Wijsian geostatistics for ore evaluation, *South African Institute of Mining and Metallurgy*, Johannesburg, South Africa.
[31] Yang CN & Lee TD (1952) Statistical Theory of Equations of State and Phase Transitions. I. Theory of Condensation, *Physical Review* 87, 404-409.
[32] Cipra BA (1987) An introduction to the Ising model, *The American Mathematical Monthly*, 94, No. 10. 937-959; http://links.jstor.org/sici?sici=0002 9890%28198712%2994%3A10%3C937%3AAITTIM%3E2.0.CO%3B2-V
[33] Binney, J.J., Dowrick, N.J., Fisher, A.J. & Newman, M.E.J., 1995. *The Theory of Critical Phenomena*, Clarendon Press, Oxford, pp464.
[34] Leary PC (2002) Numerical simulation of first-order backscattered P and S waves time-lapse seismic imaging in heterogeneous reservoirs, *Geophys. J. Int.* 148, 402–425
[35] Zimmerman RW & Bodvarsson GS (1996) Hydraulic Conductivity of Rock Fractures, Earth Sciences Division, Lawrence Berkeley Laboratory, University of California Berkeley, CA 94720
[36] Jaeger JC, Cook NGW & Zimmerman RW (2007) *Fundamentals of Rock Mechanics*, Fourth Edition Blackwell Publishing, pp488.
[37] Kwiatek G, Saarno T, Ader T, Bluemle F, Bohnhoff M, Chendorain M, Dresen G, Heikkinen P, Kukkonen I, Leary P, Leonhardt M, Malin P, Martínez-Garzón P, Passmore K, Passmore P, Valenzuela S & Wollin C (2019) Controlling fluid-induced seismicity during a 6.1-km-deep geothermal stimulation in Finland, *Science Advances* 01 May 2019: Vol. 5, no. 5, eaav7224 DOI: 10.1126/sciadv.aav7224
[38] Leary P, Malin P, Saarno T & Kukkonen I (2017) Prospects for assessing enhanced geothermal system (EGS) basement rock flow stimulation by wellbore temperature data, *Energies*, 10, 1979; doi:10.3390/en10121979
[39] Bredehoeft JD & Papaopulos IS (1965) Rates of vertical groundwater movement estimated from the Earth's thermal profile, *Water Resources Research, 1*, 325–328; doi: 10.1029/WR001i002p00325.
[40] Leary P, Malin P, Saarno T, Heikkinen P & Diningrat W (2019) Coupling crustal seismicity to crustal permeability – Power-law spatial correlation for EGS-induced and hydrothermal seismicity, 43rd Workshop on Geothermal Reservoir Engineering Stanford University, February 11-13, 2019 SGP-TR-2141.
[41] IFC (2013) *Success of Geothermal Wells: A Global Study*, International Finance Corporation, 2121 Pennsylvania Ave. NW, Washington, DC 20433.
[42] Kukkonen I & Lindberg A (1998) Thermal properties of rocks at the investigation sites: measured and calculated thermal conductivity, specific heat capacity and thermal diffusivity, Working Report 98-09e, Posiva Oy Mikonkatu 15 A, FIN-001 00 Helsinki, Finland.
[43] Clauser C (1992) Permeability of crystalline rocks, *Eos*, Vol. 73, No. 21, 237-238.

Appendix 1 – Peclet numbers for crustal heat extraction by planar flow & wellbore-centric flow

The physical scale of crustal heat extraction flow systems is set by the dimensionless Peclet number P_e, the ratio of the product of fluid flow velocity and characteristic physical scale of heat-exchange process with the thermal diffusivity of the fluid-rock system. For fracture-borne fluid flow between crustal wellbore pairs, this ratio is $P_e = v\delta/D$, for v = fluid flow velocity in the fracture, 2δ = the width of the fracture, and rock-fluid system thermal diffusivity $D \equiv K/\rho C \sim 0.7\ 10^{-6}$ m^2/s fixed by the thermal conductivity of

rock $K \sim 2.8$W/m·°C and the volumetric heat capacity of liquid water $\rho C \sim 4$MJ/m^3·°C (950kg/m^3 x 4180J/kg·°C) at depth in the crust. The thermal diffusivity of rock is $D_r \sim 2.8/(2700\text{kg/m}^3 \text{ x } 810\text{/kg·°C}) \sim 1.3\ 10^{-6}$ m^2/s. Sample thermal properties for Finnish crust are given in Fig A1-1.

For fracture-borne crustal heat extraction flow between two vertical wellbores in the y=0 plane embedded in a crustal volume of diffusivity D_r at temperature T_0, fluid moving at steady velocity v [m/s] in an aperture 2δ removes heat fluid such that crustal temperature distribution at time t and position x along the fracture and distance y into the fracture wall is given by

$$T(x,y,t) = T_1 + (T_0 - T_1)\ erf[(y+x/P_e)/\sqrt{(4D_rt)}],$$

for water injected at temperature $T_1 < T_0$ [8].

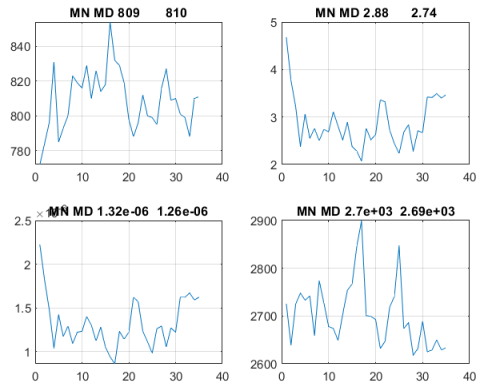

Figure A1-1: Finnish basement rock thermal property distributions from 500m depth [42]. From upper-left to lower-right: heat capacity, thermal conductivity, thermal diffusivity, and mass density. In titles, MN denotes mean value, MD denotes median value. The fact that the mean and the median values are close indicates that rock thermal properties, unlike rock flow properties, are normally distributed.

Fracture-borne water flowing into a production wellbore length ℓ at velocity v through fracture aperture 2δ with Peclet number $P_e = v\delta/D$ extracts heat rate $Q = 2v\delta\ell(\rho C)_w(T_1 - T_0) = 2P_eK\ell(T_1 - T_0)$. For a given wellbore heat production rate Q, the crustal lateral dimensions $0 < x < X$ and $0 < y < Y$ must be large enough that over time $0 < t < \tau$ the crustal heat store supplies sufficient high-temperature heat energy to cover drilling costs. For a typical wellbore heat production $Q = 30\text{MW}_{\text{th}}$ [41] extracted at temperature $(T_1 - T_0) = 200$°C along a wellbore of length $\ell = 1000$m, the fracture-flow-system Peclet number is $P_e \sim 75$. For a system of fracture-borne extraction scale $P_e \sim 75$, the length X of fluid travel along the fracture must be such that argument of the error-function argument $X/75\sqrt{(4D_rt)}$ is sufficiently large at time $\tau = 30$ years that the crustal heat is supplied at an adequate temperature. A representative value imposed by this condition is $X \sim 75\sqrt{(4D_r\tau)} \sim 4.5$km. Detailed crustal heat extraction simulations confirm the scale of these early model estimates [24-25].

Appendix 2 – Incidental rock property data in support of flow stimulation modelling

Formation Micro-Imager (FMI) logs return circum-wellbore resistivity data using multi-arm, multi-sensor-pad electrical resistivity sensors with mm-spatial resolution along the wellbore axis. FMI logs are typically used to map the orientation and dip of large-scale planar structures that intersect the wellbore. While it is commonly accepted that the identified planar structure are active fractures, a detailed look at FMI trace data suggests an alternative interpretation: that the mapped ''fractures'' are fossil structures with resistivity highs due to the low permeability of silica and calcite infill.

Fig A2-1 (left) shows a suite of eight resistivity sensor pad data recorded over a 37m interval of a North Sea reservoir formation. Data spikes attributable to wellbore intersection by planar structures are all resistivity highs rather than conductivity highs. Fig A2-1 (right) shows power-spectral scaling coefficients of order 1 for the wellbore resistivity fluctuation sequences, extending to the mm-Dm scale range the grain-scale spatial correlation empirics observed for crustal fluid-rock interactions across the m-km range.

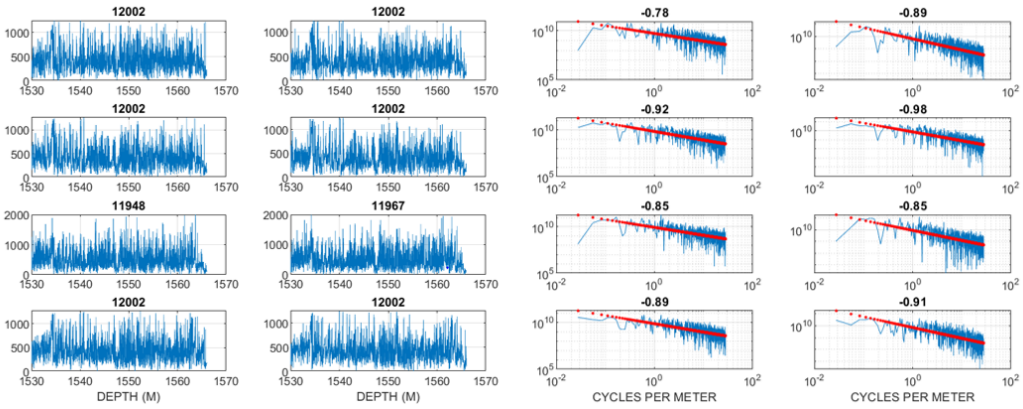

Figure A2-1: North Sea reservoir formation FMI well logs (left) and the 1/k-scaling power spectra (right).

Fig A2-2 further develops this theme. Superposition of the eight FMI resistivity traces of Fig A2-1 show the spatial correlation nature of the resistivity spikes for ambient reservoir rock between 1530m and 1565m. Low resistivity data plotted in black are largely incidental where they cluster at the low end of a resistivity structure. Deeper than 1565m, the rock section becomes highly fractured, indicated by the absence of high resistivity spikes and the dominance of low resistivity data. There is no direct evidence for conductivity spikes that might denote an open fracture.

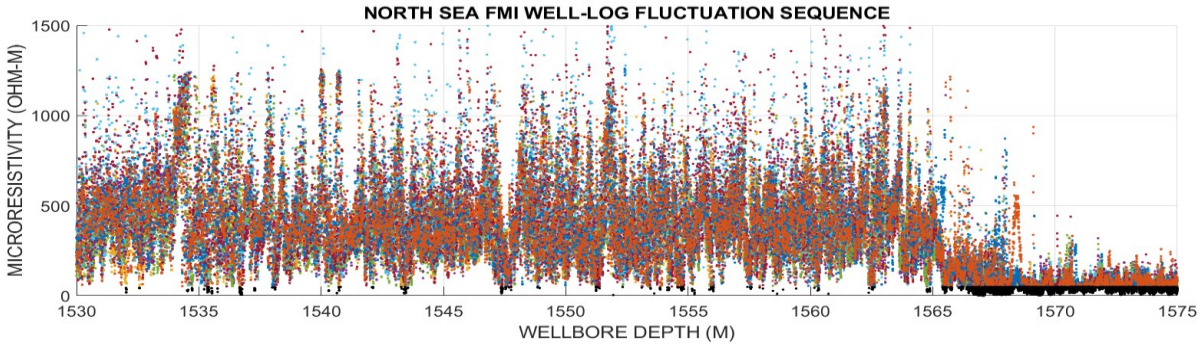

Figure A2-2: Supposition of Fig A2-1 FMI resistivity traces. Low resistivity shown in black clusters in the whole-rock section above depth 1565m; below 1565m, is a zone of highly fractured rock with low resistivity.

Figs A2-1 and A2-2 indicate that crustal fractures tend to cluster at all scale lengths rather than appear as discrete discontinuities in an otherwise quasi-uniform elastic continuum.

The median value of the Deep Heat ambient crustal permeability is given by the observed stimulation fluid influx rate $V = 2\pi r_0 \varphi v_0 \ell$ ~ 600L/min ~ 10L/s ~ 10^{-2}m^3/s [37]. For ℓ = 200 meters of open hole with nominal radius r_0 ~ .167m and mean crustal porosity φ ~ 0.01, we obtain the nominal injection fluid $v_0 \sim 5 \cdot 10^{-3}$m/s. For fluid injection into a porous medium of median permeability κ_0, the radial pressure field $P(r)=P_0 + (P_1 - P_0)log(r_0/r)/log(r_0/r_1)$ in annular zone $r_0 < r < r_1$ gives fluid velocity $v_0 = \kappa_0/\mu\ \partial_r P(r)|_{r0} \sim \kappa_0/\mu\ (-P_0/r_0/log(r_0/r_1)) \sim \kappa_0/3 \cdot 10^{-4}$ Pa·s x $2 \cdot 10^8$ Pa/m, whence for observed fluid injection velocity $v_0 \sim 5 \cdot 10^{-3}$m/s, the effective permeability is $\kappa_0 \sim 0.75 \cdot 10^{-14}$m^2. This crustal permeability value agrees with the range of values given in Fig A2-3.

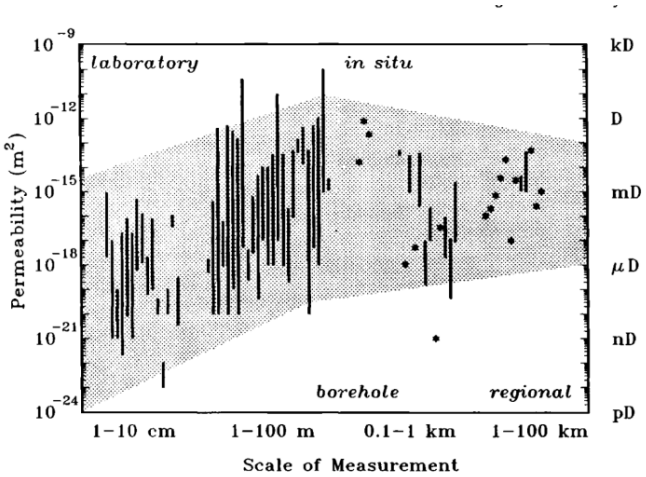

Figure A2-3: Crustal rock permeability as function of physical scale [43].